Article

Assessing the Capability of a Downscaled Urban Land Surface Temperature Time Series to Reproduce the Spatiotemporal Features of the Original Data

Panagiotis Sismanidis [1,2,*,†], Iphigenia Keramitsoglou [1,†], Chris T. Kiranoudis [1,2,†] and Benjamin Bechtel [3,†]

[1] Institute for Astronomy, Astrophysics, Space Applications and Remote Sensing, National Observatory of Athens, Athens GR-15236, Greece; ik@noa.gr (I.K.); kyr@chemeng.ntua.gr (C.T.K.)
[2] School of Chemical Engineering, National Technical University of Athens, Athens GR-15780, Greece
[3] Center for Earth System Research and Sustainability, University of Hamburg, Hamburg DE-20146, Germany; benjamin.bechtel@uni-hamburg.de
[*] Correspondence: panosis@noa.gr; Tel.: +30-210-810-9167
[†] These authors contributed equally to this work.

Abstract: The downscaling of frequently-acquired geostationary Land Surface Temperature (LST) data can compensate the lack of high spatiotemporal LST data for urban climate studies. In order to be usable, the generated datasets must accurately reproduce the spatiotemporal features of the coarse-scale LST time series with greater spatial detail. This work concerns this issue and exploits the high temporal resolution of the data to address it. Specifically, it assesses the accuracy, correct pattern formation and the spatiotemporal inter-relationships of an urban three-month-long downscaled geostationary LST time series. The results suggest that the downscaling process operated in a consistent manner and preserved the radiometry of the original data. The exploitation of the data inter-relationships for evaluation purposes revealed that the downscaled time series reproduced the smooth diurnal cycle, but the autocorrelation of the downscaled data was higher than the original coarse-scale data. Overall, the evaluation process showed that the generation of high spatiotemporal LST data for urban areas is very challenging, and to deem it successful, it is mandatory to assess the temporal evolution of the urban thermal patterns. The results suggest that the proposed tests can facilitate the evaluation process.

Keywords: thermal remote sensing; urban heat island; land surface temperature; LST downscaling; evaluation; diurnal evolution; hotspots; MSG-SEVIRI; MODIS

1. Introduction

The Urban Heat Island (UHI) is one of the most representative manifestations of climatic modification [1,2]. This effect refers to the relative warmth of urban areas with respect to their surrounding rural areas and is present in every city and town. UHIs are primarily caused by the alteration of the urban local climate and heat balance due to the large-scale conversion of pervious surfaces to impervious surfaces and also the increased anthropogenic heat fluxes of urban areas [1]. UHIs exhibit strong spatial, temporal and vertical variations and have been related to a range of issues, such as human health and energy demand [3–5]. Their impact is expensive [6] and extends to large populations and areas [5].

Due to their importance, the study of UHIs has concerned the scientific community for more than 50 years. Most relevant studies employ *in situ* Air Temperature (TA) data [1,7–12]. After 1972, remotely-sensed Land Surface Temperature (LST) data have also been utilized for the study of the

Surface UHI (SUHI) [13–16]. In contrast to TA data, which are point measurements confined to local conditions [17], thermal infrared (TIR) remote sensing is capable of providing a simultaneous and synoptic view of the urban thermal environment [18]. This enables the more detailed assessment of the urban hotspots and the relationship between the urban core and the surrounding natural lands [18–20]. Nevertheless, the use of satellite TIR data is not straightforward, and a number of limitations and problems, such as the atmospheric influence, the unknown emissivity and the effective anisotropy, have to be addressed prior to their exploitation [21]. To that end, one of the most important problems concerns the spatial and temporal resolution of the LST data. In particular, the available satellite sensors cannot provide datasets that capture the high spatial and temporal variability of SUHIs, and thus, their exploitation in urban climate studies is limited [22–25]. For instance, the Sun-synchronous Landsat series satellites, which offer the appropriate high spatial resolution (~100 m), acquire LST data every 16 days; whereas the Spinning Enhanced Visible and Infrared Imager (SEVIRI) onboard Meteosat Second Generation (MSG) geostationary satellites provides ~4 km TIR data with a more appropriate temporal resolution of 5–15 min.

To overcome this problem, the statistical downscaling of geostationary LST data has been proposed. This process can lead to the generation of Downscaled LST (DLST) time series that combine high spatial and temporal resolution and preserve the radiometry of the original thermal data [22–26]. In detail, the LST statistical downscaling is a scaling process that aims to enhance the spatial resolution of coarse-scale LST imagery using fine-scale auxiliary datasets. These auxiliary datasets are usually referred to as LST predictors and are statistically correlated to the LST [26]. An LST downscaling scheme comprises two major parts. The first part is the set of LST predictors used for explaining the spatial variation of LST, while the second part is the regression tool used for associating the LST predictors with the LST data. These two parts are synergistically exploited in a three-stage procedure: firstly, the LST predictors are upscaled and co-registered to the coarse-scale LST data; then, a relationship between the coarse-scale LST data and the LST predictors is established using the regression tool; and finally, this relationship is applied to the fine-scale LST predictors, so as to generate the DLST data. Agam *et al.* [27] and Kustas *et al.* [28] include also a fourth process stage, which is an adjustment of the generated DLST data based on the differences of the observed and regressed coarse-scale LSTs. This post-downscaling processing aims to compensate the loss of LST variability due to the use of inflexible regression tools, such as least-square or linear fits [28].

In recent years, a large number of relevant works have been published [26] testing different LST predictors (separately or combined), such as: Vegetation Indices (VIs), emissivity data, land cover maps and topography data; and also regression tools, such as: linear regressors, least-square fits, Support Vector Regression Machines (SVMs) and Neural Networks (NNs) [22–29]. From the available list of LST predictors, the most widely used is the Normalized Vegetation Difference Index (NDVI) [27–29], which is strongly negatively correlated with summer daytime LST imagery [30]. Most of the aforementioned works focus on the downscaling of ~4 km data down to 1 km. The downscaling to even higher spatial resolutions (<500 m) is still a very challenging task, mainly because the assumption that the LST data-predictor relationship is valid in both spatial scales weakens or ceases to apply [31]. The work of Bechtel *et al.* [24] is one of the few studies that discusses the downscaling of geostationary urban LST data down to 100 m with a Root-Mean-Square-Error (RMSE) of 2.2 °C (recent LST fusion studies [32,33] also report similar downscaling factors). In this work, a large set of LST predictors was utilized that also included for the first time LST annual climatology data in the form of annual cycle parameters (ACPs) [34–36]. The use of the ACPs for downscaling LST data below the 1-km cap provided very promising results [24]. However, this type of LST predictor has not been used as extensively as the rest, and thus, the available relevant literature is still very limited.

Besides the identification of more robust predictors, another issue that requires attention is the evaluation of the generated high spatiotemporal DLST time series, which is hampered by the lack of appropriate ground truth data [21]. Presently, most downscaling studies utilize independent LST image data (confined to certain time spots) with which they compare the generated data and

calculate statistical measures of accuracy and similarity. However, this approach is quite limiting when evaluating DLST time series. This is because it does not examine if the downscaling process was capable of accurately reproducing the spatiotemporal features of the original LST time series (with greater spatial detail), e.g., the SUHI diurnal cycle, and their spatiotemporal inter-relationships (the 5–15-min acquisition cycle makes the relationships between sequential DLST data especially pronounced). A review of the relevant literature reveals the following gaps regarding the evaluation of DLST data/time series:

- Limited sample dataset used for evaluating the proposed methods. Currently, the evaluation of the main bulk of available downscaling algorithms has been restricted to a small sample of scenes. However, this approach does not allow the assessment of the method's consistency, robustness and reliability, which are also important. This is because the proposed LST downscaling algorithms will eventually be applied to LST time series and not only to individual scenes.
- The in-depth evaluation of the revealed DLST spatial thermal patterns. The extraction of spatial information from LST images is a major input, especially for SUHI studies [20]. The shape of the revealed DLST hotspots is heavily dependent on the set of LST predictors used. In detail, the downscaling of the same coarse-scale LST time series, with the same regression tool, but with different sets of LST predictors, would lead to the formation of different DLST spatial patterns.
- The assessment of the spatiotemporal inter-relationships between sequential DLST data. The diurnal evolution of the LST (and TA) follows a sine wave-like pattern where the LST values smoothly increase during daytime and smoothly fall during nighttime. Short-term weather effects (e.g., heatwaves) and seasonal effects (e.g., vegetation phenology) affect this sine wave-like pattern. In LST time series, the impact of these effects is recorded as special time-dependent features [37]. The features caused by short-term weather effects are presented as brief, but pronounced changes in LST values and patterns. For instance, a heatwave is recorded as an increase of LST values and an intensification of the SUHI spatial cluster for a number of consecutive days [38,39]. On the other hand, the seasonal effects are more subtle and only observable when examining long time series, e.g., the gradual cooling from summer to winter. Hence, a successful downscaling of LST time series should result in a smooth diurnal evolution of DLST values and patterns and emulate the short-term and seasonal features of the coarse-scale LST time series.
- Assessment of the downscaling method's performance for different biomes, seasons and topographic and climatic conditions. This issue is important because these factors might influence the relationship between the LST data and the LST predictors and, thus, impact the downscaling process by rendering some LST predictors less effective or even ineffective for certain conditions. For instance, the correlation between NDVI and LST weakens during autumn months [30] and depends also on vegetation type/latitude [40].

This work concerns the first three issues presented above through the study of a downscaled three-month long MSG3-SEVIRI LST time series depicting Rome, Italy. In particular, it assesses the accuracy and correct pattern formation of the generated DLST data and also the impact of the downscaling process on the diurnal evolution of the DLST urban and rural spatial patterns. The assessment process is based firstly on comparisons with an independent LST time series from the Moderate Resolution Imaging Spectroradiometer (MODIS) and secondly on the estimation of autocorrelation measures that exploit the high temporal resolution of the MSG3-SEVIRI data. This article proceeds as follows: in Section 2, the study area and the employed LST data and predictors are presented. In Section 3, the generation of the MSG3-SEVIRI DLST data and the performed evaluation tests are discussed, while in Section 4, the results obtained are presented. The article concludes with a review of this study's contribution and novelty.

2. Study Area and Data

2.1. Study Area

This work focuses on the city of Rome and the surrounding rural region (Figure 1). The city of Rome is the capital of Italy. It is located in the central-western Italian Peninsula and has a population of ~3.7 million people. The study area extends to approximately 60 km around Rome and covers an area of 10,350 km^2. From those, ~50% correspond to agricultural lands, ~40% to vegetated lands and ~10% to urban areas (Figure 1b). The elevation of the area under study varies from 0–1.5 km (Figure 1c). The eastern part of the study area, where the Apennine Mountains are located, is the region with the highest altitude and the most pronounced topographic features. The city of Rome is enclosed in a valley surrounded by the Apennine Mountains, with a lower elevation (13–120 m) and a more subtle topography (Figure 1c). The different nature of these two areas is reflected in the formed spatial thermal patterns, as evident in Figure 1d (Pattern 1: Apennine Mountains; Pattern 2: rural area surrounding Rome; Pattern 3: city of Rome).
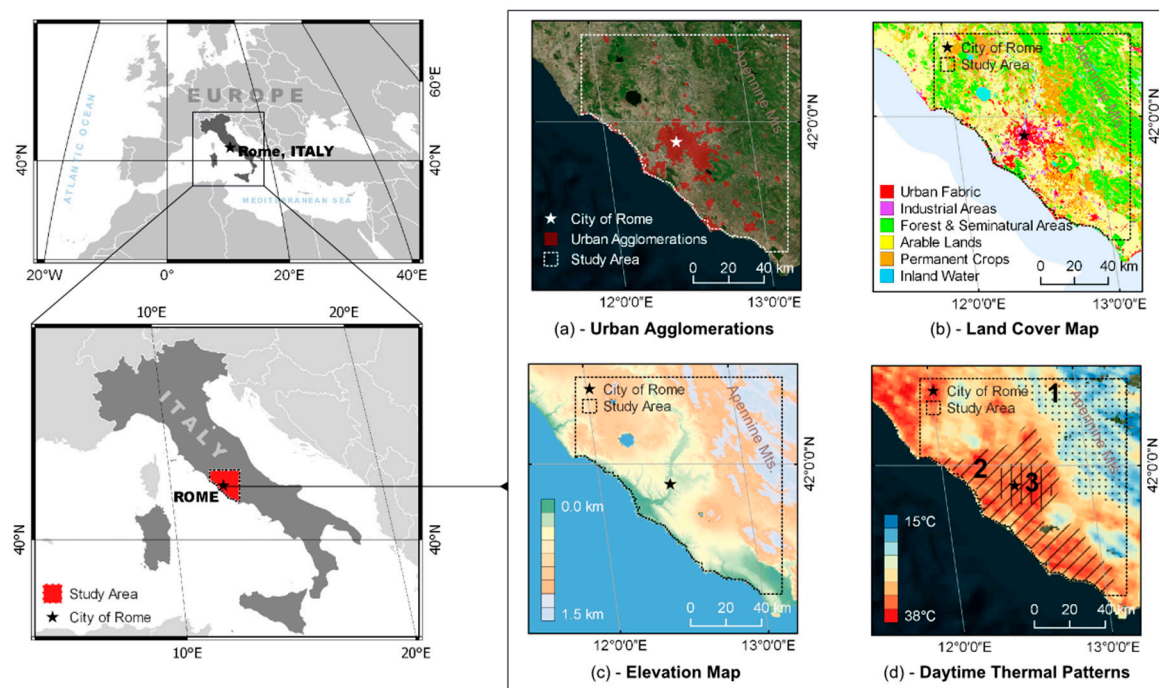

Figure 1. (**a**) The urban agglomerations located inside the study area; (**b**) the corresponding CORINE 2006 land cover map; (**c**) the elevation map of the study area; (**d**) characteristic 10:30 UTC daytime 1-km LST spatial patterns as observed by MODIS (1: Apennines; 2: rural area surrounding Rome; 3: city of Rome).

2.2. LST Data

This study exploits two different time series of satellite LST image data that depict the exact same region (Figure 1) and cover the same time period (Summer of 2014, DOY: 152–243). The first time series was retrieved from MSG3-SEVIRI (as discussed in [17,41]) and was the main input in the downscaling process. The second dataset was obtained from the available cloud-free MODIS MOD11A1 and MYD11A1 Version 5 data products and served as the independent evaluation dataset for the generated 1-km MSG3-SEVIRI DLST data. The two time series have different spatiotemporal characteristics: MSG3-SEVIRI offers 4 × 5-km LST data 96 times every day (one image every 15 min), whereas MODIS provides 1-km LST data four times every day (two at noon: ~10:30 and ~12:30 UTC; and two at night: ~01:30 and ~21:30 UTC; morning and afternoon data are not available). The two time series have also

different acquisition geometries. In particular, MSG3-SEVIRI acquires data of the study area with a constant view zenith angle (VZA) equal to +50° and an azimuth angle equal to 18.4°, whereas MODIS with a VZA that ranges from −55°−+55° (the "+" sign means that the sensors view the area beneath from the west, while the "−" sign from the east [42]). In this study, only MODIS data acquired with a positive VZA were considered. This was done so as to avoid any comparisons between inconsistent LST data [21,42], *i.e.*, LST data where the ensemble of surfaces sampled by the two satellite sensors would dramatically differ due to the opposite observation geometries. The selection of only MODIS data with a similar VZA to MSG3-SEVIRI was not considered as an option, because the evaluation dataset would become too limited for the time period under study. Eventually, 6470 MSG3-SEVIRI (on average, 71 images per day; only images with a <30% cloud cover were retained) and 92 MODIS (47 daytime and 45 nighttime) LST images were retrieved. The time distribution of the utilized satellite LST data is presented in Figure 2. The data collected are well distributed throughout the 2014 summer months and also throughout each day with some exceptions due to high cloudiness [17]. In most cases, two MODIS images were available for each day, covering sufficiently the time span of interest (MODIS data were available for 50 of the 90 days covered by this study).
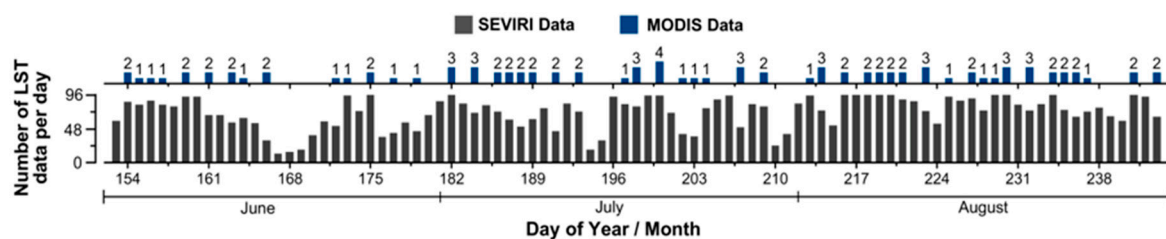

Figure 2. The time distribution of the employed MSG3-SEVIRI and MODIS LST data.

2.3. LST Predictors

Seventeen widely-used LST predictors were utilized in this study for the downscaling of the MSG3-SEVIRI time series (Table 1). The utilized LST predictors include topography data, land cover maps, emissivity data, VIs and LST annual climatology data (*i.e.*, the ACPs). The LST predictors were selected based on previous works of the authors [23,24]. Specifically, the topography data were retrieved from the Shuttle Radar Topography Mission (SRTM; [43]) and consist of the altitude, the slope and the aspect maps (in the present study, four aspect maps were generated, one for each of the four main directions: north, south, west and east). The land cover data were obtained from the GlobCover dataset [44], which was aggregated to four major classes, water bodies, urban areas, agricultural areas and vegetated regions, and then decomposed to provide the percentages of specific land cover for each pixel. The emissivity data were retrieved from the TERRA MODIS eight-day 11-μm and 12-μm emissivity product (MOD11A2), while the VIs from the TERRA MODIS 16-day NDVI and Enhanced Vegetation Index (EVI) indices (MOD13A2). Lastly, the ACPs [34,35] were estimated from a five-year time series (2009–2013) of MODIS LST data. The LST climatology is annually periodic and can be approximated by a series of harmonic functions [34]. The ACPs' methodology exploits this attribute in a pixel-wise manner using a sine function plus a constant term that transforms into a set of five components [35]. These components are: the Mean Annual Surface Temperature (MAST, *i.e.*, the constant term); the Yearly Amplitude of Surface Temperature (YAST, *i.e.*, the amplitude of the sine function); the phase shift of the sine function (θ); the fit RMSE; and lastly, the number of observations used for the fit. In this study, the estimation of the ACPs was performed separately for TERRA and AQUA data and for daytime and nighttime data. In total, four ACP sets were obtained (one for each MODIS overpass time), from which only the MAST, YAST and θ components were included in the downscaling process. Finally, all LST predictors were (if needed) resampled to 1 km and re-projected to the MODIS sinusoidal map projection.

The aforementioned predictors correspond to two major categories: the time-independent (static) predictors and the time-dependent (dynamic) predictors. The topography data, as well as the land cover maps fall in the first category, while the rest of the predictors fall in the second category. The time-dependent predictors can be divided further into: those that change on an eight-day or 16-day basis (the emissivity and the VIs) and those that change within a day (the ACPs).

Table 1. The LST predictors employed in this study.

Type	LST Predictors
Topography Data	Altitude, slope, aspect N, aspect S, aspect W and aspect E
Land Cover Data	Water bodies, urban areas, agricultural areas, and vegetated areas
Emissivity Data	8-day 11-μm and 12-μm emissivities (MOD11A2)
Vegetation Indices	16-day NDVI and EVI (MOD13A2)
LST Annual Climatology Data	YAST, MAST and θ

3. Method

3.1. SVM-Based DLST Data Generation

The downscaling of the employed 4-km MSG3-SEVIRI LST time series was performed using the method presented in [23] and evaluated in [17], which employs an SVM coupled with gradient boosting. The SVM was preferred over other methods, because it has limited requirements on training dataset size and quality; it is effective in terms of noise reduction and computation efficiency; and its self-adaptability makes it better suited to describe the complex relationship that connects the LST data with the LST predictors [25,45]. The gradient boosting method [23], which is a machine-learning concept that combines the results of a series of model runs (or even different models) so as to form a much stronger regression model, was employed in order to improve the performance of the SVM.

The implemented workflow follows the standard three-stage procedure presented in the Introduction (*i.e.*, upscaling and coregistration; regression; generation of DLST data) and was applied to each one of the employed 6470 MSG3-SEVIRI LST images, separately. In particular, the upscaling and co-registration of the 1-km LST predictors to the 4-km MSG3-SEVIRI LST data was performed using an intermediate 1-km grid that assigned which 1-km pixels belong to each 4×5-km MSG3-SEVIRI pixel. This was performed on the basis of the coarse-scale pixel's geographical coordinates. The aggregated 4-km LST predictors were then estimated as the mean of the selected 1-km pixels, with the exception of slope and aspect maps that were re-calculated from the aggregated altitude map. Prior to upscaling, all LST predictors were min-max normalized between −1 and 1, so as to have comparable values. The last two stages of the downscaling process were the training of the regression model and the estimation of the 1-km DLST data, respectively. A 3×3 averaging filter was also applied to the generated 1-km DLST image data, so as to make them more physically realistic and to remove any artifacts.

The time dependency of the LST predictors used in this study was also taken into consideration during the downscaling process. In particular, the emissivity data and the VIs were updated every 8 and 16 days, respectively; while the ACPs were successively changed on a daily basis (the AQUA nighttime ACPs were set in use at 23:30 UTC, the TERRA daytime at 06:00 UTC, the AQUA daytime at 11:30 UTC and, lastly, the TERRA nighttime at 17:30 UTC). To that end, the estimation of intermediate ACPs from other satellite data was not possible, while the option to estimate intermediate ACPs as the average of consecutive ACPs was omitted because this would not be valid. The sequential change of the ACPs is expected to raise two problems: (i) the sudden change of the ACPs will affect the smooth evolution of the DLST spatial patterns; and (ii) the use of the night and noon ACPs during morning and afternoon hours will bias the formed DLST spatial patterns for these time periods. Nevertheless, the inclusion of the ACPs was considered significant because, being derived from fine-resolution TIR data, they will be able to explain much of the LST spatial variance and facilitate the formation of correct DLST spatial patterns. In addition, the use of a large number of diverse predictors in conjunction with

the SVM is expected to minimize the aforementioned problems (for assessing this issue, targeted tests have been performed; see Section 4.2).

3.2. Assessment of Generated DLST Time Series

The assessment of the generated DLST time series addresses the first three issues raised in the Introduction regarding the capability of the DLST time series to reproduce the spatiotemporal features of the original coarse-scale LST time series with greater spatial detail:

- Issue 1: the assessment of the method's accuracy, reliability and consistency.
- Issue 2: the evaluation of the formed DLST spatial patterns.
- Issue 3: the assessment of the potential of the generated DLST time series to emulate the diurnal and seasonal characteristics of the original LST time series.

To address each issue, a set of relevant key aims was identified (Table 2) and targeted tests were devised as discussed below. These tests are based either on the LST cross-validation method [21] or the exploitation of the high temporal resolution of the employed LST/DLST time series; and utilize either the 1-km MODIS data or the original 4-km MSG3-SEVIRI LST data, since no ground truth measurements were available. The LST cross-validation method is a widely-used [17,22–25] LST evaluation method that can be applied anywhere in the world on the condition that independent high-quality LST image data are available [21]. This method is especially advantageous to alternatives, such as the ground-based temperature-based method [21], since the availability of ground truth LST data around the globe is extremely limited. It has to be stressed though that the cross-validation, which is essentially an image-to-image comparison method, is very sensitive to spatial and temporal mismatches between the compared datasets [17,21]. In this study, the impact of these mismatches could only be minimized and not compensated completely: the compared data have the same map projection and similar acquisition time (maximum deviations less than 5–10 min), but not always the same VZA (as discussed in Section 2.2).

Table 2. The identified key aims to assess each issue and the tests performed (# is the test serial number).

Issue	#	Aim	Tests
	1	Quantification of differences between MSG3-SEVIRI DLST-MODIS LST time series.	Statistical measures at fine resolution (1 km).
Issue 1	2	Downscaling performance with respect to land cover type.	RMSE spatial distribution.
	3	Downscaling method's consistency assessment.	Image-to-image analysis between MSG-SEVIRI DLST-MODIS LST.
	4	Assessment of DLST when no coincident MODIS data are available.	Statistical measures at original resolution (4 km).
	5	Assessment of formed pattern's shape, size and location.	DLST and MODIS LST Local Moran Indices (LMI) comparison.
	6	Compliance of DLST and original LST pattern diurnal evolution.	LMI juxtaposition and visual inspection.
Issues 2 & 3	7	Magnitude of diurnal spatial change.	Similarity between the first image of the day and the remaining 95.
	8	Smoothness of DLST diurnal spatial change/artifact formation due to ACPs' sudden change.	Similarity between sequential quarter-hourly images.
	9	Preservation of original radiometry.	Min/mean/max LST-DLST value comparison.
	10	DLST potential to emulate the spatial changes due to seasonal effects.	Similarity between sequential images.

3.2.1. Accuracy and Consistency Assessment Tests Using a Long Time Series of LST/DLST Data

For addressing the first issue, four major tests were performed: (i) the quantification of the 1-km MSG3-SEVIRI DLST and MODIS LST time series differences; (ii) the assessment of the RMSE spatial distribution; (iii) the estimation of the downscaling method's performance on an image-to-image basis; and (iv) the comparison of the generated DLST data with the original MSG3-SEVIRI LST data, upscaled to 4 km.

For quantifying the differences between the 1-km MSG3-SEVIRI DLST and MODIS LST time series, several descriptive statistical measures, namely mean difference, Standard Deviation (SD), variance, RMSE and Pearson's correlation coefficient (Rho), were calculated. This analysis was performed separately for each one of the four MODIS overpass times and utilized only the MODIS pixels where the LST retrieval accuracy is equal to or better than 1 °C (the accuracy information was extracted from the MODIS quality assurance layer supplied with each MOD11A1 and MYD11A1 LST product).

In addition to the above, the RMSE spatial distribution was also estimated for each MODIS overpass time. This test aims to assess the downscaling performance with respect to land cover type; to highlight the differences between the daytime and nighttime data; and to identify any regions with persistently high RMSE. The third test was the assessment of the methods' reliability and consistency. For this purpose, the RMSE and Rho values were estimated separately for the 47 daytime and 45 nighttime MODIS-coincident DLST data, and the consistency with time was examined. The last test for addressing Issue 1 was the comparison of the generated DLST data with the original 4-km MSG3-SEVIRI LST time series. For this purpose, all 6470 MSG3-SEVIRI images were employed, and several statistical measures were calculated. In particular, the DLST data were upscaled to 4 km using the method discussed in Section 3.1 and then divided into 96 groups (corresponding to each MSG3-SEVIRI quarter-hourly acquisition time). For each group, the distribution of LST differences, the mean value, the RMSE and the Rho statistical measures were computed.

3.2.2. Test for the Assessment of the Formed Spatial Patterns

The assessment of the formed DLST spatial patterns is required, since the SVM can form unwanted artifacts. To facilitate the assessment of the spatial thermal patterns, the Local Moran Index (LMI; [46]) was employed, which is an established spatial analysis tool for the detection of spatial clusters. The LMI identifies the prevalent hotspots by comparing individual locations with their neighborhood using Equation (1). In Equation (1), z_i is the pixel value at location i, m_2 is the second moment as an estimate of variance, w_{ij} is a distance-based weight for pixel j included in the neighborhood of pixel i and n is the sample number. The application of the LMI leads to the generation of a new image depicting the prevalent thermal patterns.

$$LMI_i = \frac{z_i}{m_2} \sum_j w_{ij} z_j, \text{ where } m_2 = \sum_i \frac{z_i^2}{n} \tag{1}$$

To assess the formed spatial patterns, the MSG3-SEVIRI DLST-derived LMI images were compared to the corresponding daytime and nighttime MODIS LMI. Specifically, the three-month mean, MODIS-coincident DLST images were estimated and then employed for calculating the LMI. This was done so as to minimize the influence of local short-term weather effects. The evaluation of the retrieved LMI was performed by comparing the location, the shape and the size of the prevalent thermal clusters with the ones derived from the MODIS data.

3.2.3. Tests for Assessing the DLST Diurnal and Seasonal Features

For addressing the third issue, three tests were performed. The first test concerns the assessment of the spatial pattern diurnal evolution. For this test, the 6470 MSG3-SEVIRI images included in each dataset (*i.e.*, the 4-km LST and the 1-km and 4-km DLST time series) were divided into 96 groups (according to their acquisition time) and averaged. Then, the LMI was calculated separately for each

three-month mean image to minimize the weather effects. The analysis of the retrieved LMI data was performed in three stages. Firstly, the 1-km DLST-derived LMI data were juxtaposed with the corresponding 4-km LST-derived LMI data for assessing the agreement of the corresponding spatial patterns. Then, the magnitude of the spatial pattern diurnal change was examined by calculating the Rho between the 00:00 UTC image with each one of the following 95 (similar to Figure 3a; the 4-km LST data acted as a reference). Finally, the smoothness of the diurnal DLST pattern evolution was assessed by estimating the Rho between sequential quarter-hourly images (similar to Figure 3b). In particular, it was assumed that the 15-min MSG3-SEVIRI data acquisition frequency is too short for any major spatial pattern change to take place. Hence, the Rho between sequential quarter-hourly mean LST/LMI data should be close to 1. The impact of the sudden ACPs change was also assessed using the aforementioned autocorrelation tests.

Figure 3. A graphical representation of the autocorrelation tests performed for assessing the spatiotemporal features of the DLST time series: (**a**) estimation of Rho between the first image of the set and the rest; and (**b**) estimation of Rho between sequential images.

For the second test, the 1-km mean, minimum and maximum DLST values of each generated image were compared to the corresponding 4-km LST values so as to assess if the original radiometry is preserved. The third test focuses on the spatial changes due to seasonal effects. In detail, it was assumed that for a long, but finite time period, as the period under study, the Rho between the first MODIS image (*i.e.*, the one acquired first) and each one of the rest (in a sequential manner similar to Figure 3a) should exhibit a smooth declining trend. This trend would be due to seasonal effects, and the DLST data should replicate it.

4. Results and Discussion

4.1. Accuracy and Consistency Assessment

4.1.1. Comparison of Corresponding 1-km MSG3-SEVIRI DLST and MODIS LST Time Series

The first aim of the evaluation process is to provide an accuracy estimation of the retrieved 1-km DLST data through comparisons with the corresponding MODIS LST data. The results (Table 3; Figure 4) are consistent between day- and nighttime. The mean difference is close to $-0.3\ ^{\circ}$C in almost every case, with the exception of the 10:30 UTC data, where the MSG3-SEVIRI DLST time series is warmer by $+1.1\ ^{\circ}$C. Furthermore, the calculated LST differences are more dispersed for daytime (SD of ~3.1 $^{\circ}$C) than for nighttime (SD of ~1.2 $^{\circ}$C) data. The superiority of nighttime results, which is a trend reported in most downscaling works (e.g., [22]), is also evident for RMSE (~3.1 $^{\circ}$C for daytime and ~1.3 $^{\circ}$C for nighttime). Rho is equal to ~0.86 for daytime and ~0.9 for nighttime comparisons.
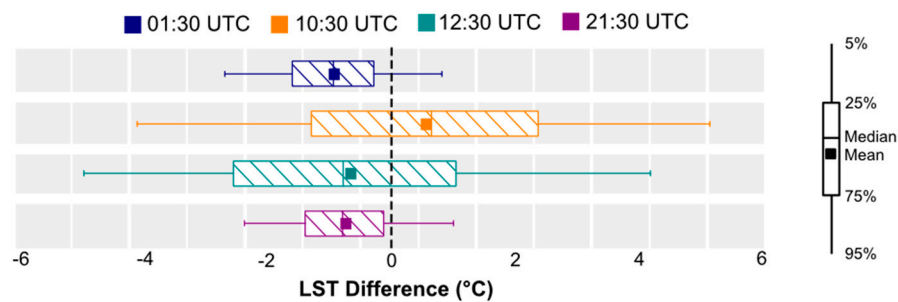
Figure 4. The distribution of the LST differences between the generated 1-km DLST and reference LST datasets.

Table 3. The results of the MSG3-SEVIRI DLST-MODIS LST time series comparison.

Statistical Measures	01:30 UTC	10:30 UTC	12:30 UTC	21:30 UTC
Mean Difference	−0.46	+1.10	−0.20	−0.25
Variance	1.41	9.10	8.96	1.38
SD	1.19	3.02	2.99	1.18
RMSE	1.27	3.21	3.00	1.20
Rho	0.88	0.85	0.86	0.91

4.1.2. Analysis of RMSE Spatial Distribution

The performance of the downscaling process is not the same for every pixel, but depends on land cover type and topography [42]. To assess this issue, the spatial distribution of the RMSE for each MODIS overpass time is presented in Figure 5. From Figure 5, it is evident that every pixel, regardless of land cover type, has a higher RMSE in daytime than in nighttime and that the daytime RMSE spatial patterns are considerably more complex than the nighttime (in accordance with [42]). In particular, the Apennine Mountains (Pattern 1 of Figure 5) daytime and nighttime RMSE values are ~6.0 °C and ~1.0 °C, respectively, making it the most pronounced daytime spatial feature. For Rome (Pattern 3 of Figure 5), the corresponding RMSE values are ~3.5 °C and ~2.5 °C, respectively, and it is the most prominent nighttime feature. The rural area pixels exhibit the lowest RMSE values (~2.0 °C for daytime and ~1.0 °C for nighttime).
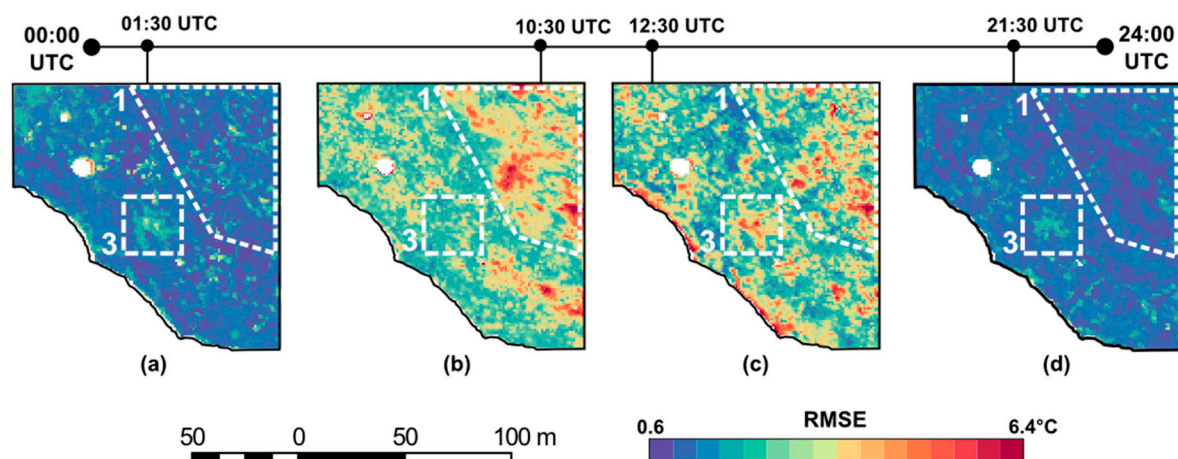

Figure 5. The (**a**) 01:30 UTC; (**b**) 10:30 UTC; (**c**) 12:30 UTC; and (**d**) 21:30 UTC RMSE spatial distribution of the generated DLST dataset for each MODIS overpass time. The outlined Areas 1 and 3 correspond to the Apennines and Rome, respectively.

The particularly high daytime RMSE values over the Apennines (Figure 5) are mostly due to colocation uncertainties [42] and the enhanced effective anisotropy of rugged terrain [47]. Specifically, the terrain-induced shadows cause differential heating patterns that increase the spatial heterogeneity of the LST. The enhanced LST spatial heterogeneity makes the emitting surfaces differ even more when viewed at different angles, as is the case between MSG3-SEVIRI and MODIS (Section 2.2). Hence, the radiometric incompatibilities between the same rugged-terrain pixels are more pronounced and lead to the calculation of higher RMSE values with respect to flat regions. The influence of shadows on effective anisotropy can also explain why the daytime Apennines' RMSE patterns are more pronounced for the 10:30 UTC data than the 12:30 UTC data. In particular, the increase of Sun elevation from ~50°–~70° during the 10:30–12:30 UTC period implies that the differential heating patterns caused by the Sun-terrain geometric configuration become weaker with time. Hence, their influence decreases during the 10:30–12:30 UTC time period, and so do the radiometric incompatibles between MSG3-SEVIRI and MODIS for this region.

4.1.3. Assessment of the Downscaling Method's Stability and Consistency

The image-to-image RMSE and Rho values for assessing the downscaling method's stability and consistency are presented in the scatterplots and frequency histograms of Figure 6. Specifically, the calculated Rho values are greater than 0.7 for 86 of the available 92 MODIS-MSG-SEVIRI pairs (only for three daytime and the nighttime images the Rho was lower than 0.7); and the RMSE is consistently close to 3 °C for daytime and 1 °C for nighttime comparisons. Hence, the performance of the downscaling method is considered consistent.
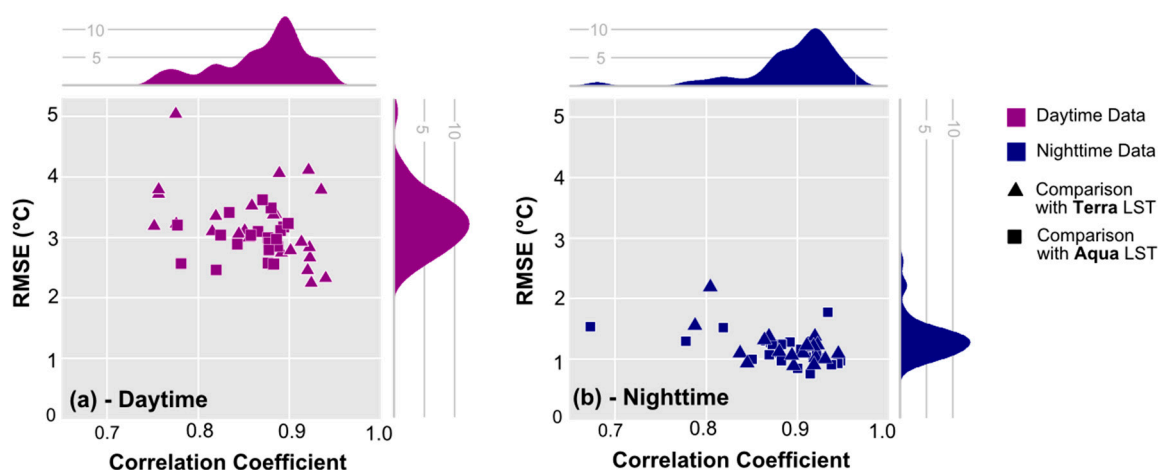

Figure 6. The RMSE and the correlation coefficient of the SEVIRI DLST that were compared to the MODIS (**a**) daytime and (**b**) nighttime data. The corresponding RMSE (vertical) and correlation coefficient (horizontal) frequency histograms are included for each plot.

4.1.4. Comparison of MSG3-SEVIRI LST and DLST Time Series

The hourly distribution of the LST differences between the original 4-km MSG3-SEVIRI LST and the upscaled DLST time series is presented in Figure 7a, while the corresponding Rho and RMSE values are presented in Figure 7b,c, respectively. The mean LST difference (bias) is close to 0 °C for all time spots under study, while the SD of the LST differences is greatest for the 10:00–14:00 UTC time period and minimum for the 00:00–09:00 UTC and the 17:00–24:00 UTC time periods. The RMSE shows a similar pattern: the RMSE is equal to ~1 °C in the morning hours until 09:00 UTC, and then, it starts increasing. At 14:00 UTC, it reaches its maximum value (~1.8 °C) and then starts to fall back to ~1 °C. Rho is close to 0.9–0.95 almost throughout the day, with the exception of noon, when it falls

to 0.85. Consequently, it can be assumed that the performance of the downscaling process during morning and afternoon hours would not be as good as for night hours, but better than noon.
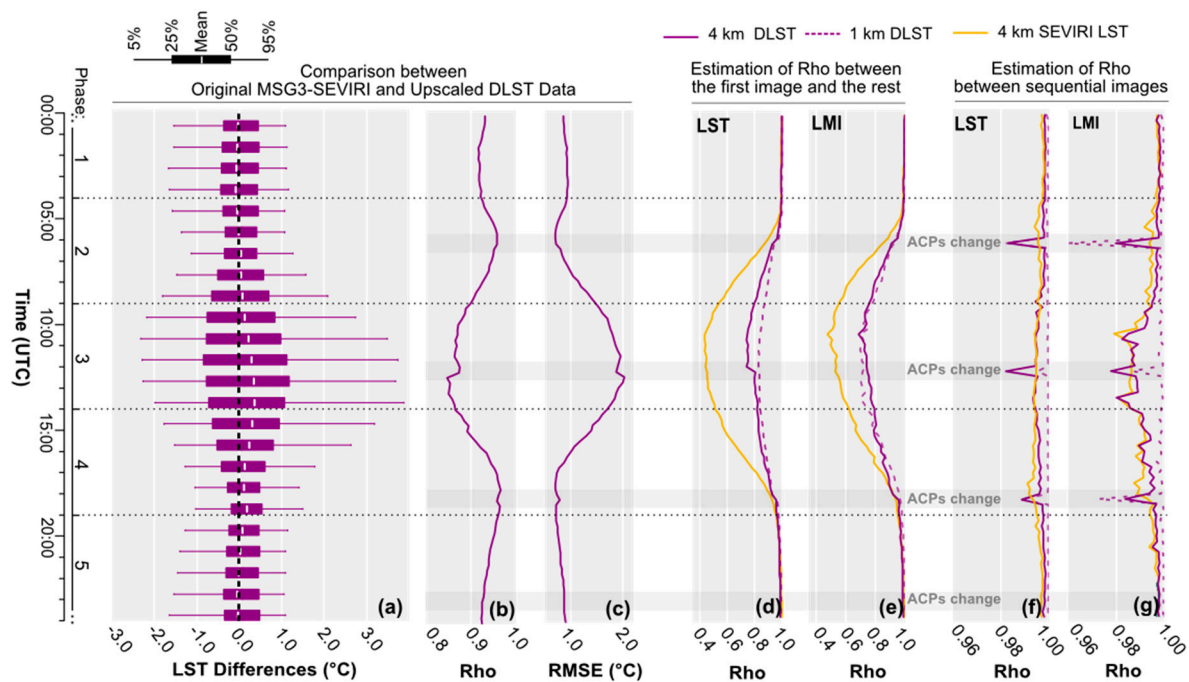

Figure 7. The (**a**) mean difference and the distribution of LST differences, (**b**) Rho and (**c**) RMSE between the DLST (upscaled to 4 km) and original coarse-scale MSG3-SEVIRI LST data; the Rho between the first mean (**d**) LST and (**e**) LMI image and the rest (both for 4 km and 1 km); the Rho between sequential mean (**f**) LST and (**g**) LMI images (both for 4 km and 1 km).

4.2. Assessment of Formed Spatial Patterns

In Figure 8, the predominant spatial thermal clusters as derived by the 10:30 UTC and 21:30 UTC MODIS and the corresponding DLST data are presented, respectively (the 12:30 and 01:30 UTC data were bypassed because the spatial patterns are similar to the above). In general, the same major clusters are present between the MODIS LST and MSG3-SEVIRI DLST data. However, none of the DLST images emulates the spatial features visible in the MODIS LST data with the same sharpness and contrast; they appear somewhat blurry.

The high homogeneity of the DLST data affects the extraction of spatial information from the generated data. In this work, the high similarity of adjacent DLST pixels led to the estimation of larger LMI clusters and higher LMI values and, thus, to the extraction of larger hotspots. This is evident especially for the daytime data (Figure 8a), where the dominant MODIS LMI (orange shapes) and MSG3-SEVIRI DLST LMI (blue shapes) hotspots differ in size (Figure 8a). For the 21:30 UTC data (Figure 8b), the blurriness impact is minor, since the nighttime LST values are intrinsically homogeneous. In general, the nighttime LMI-derived MODIS and MSG3-SEVIRI hotspots are similar (Figure 8b).
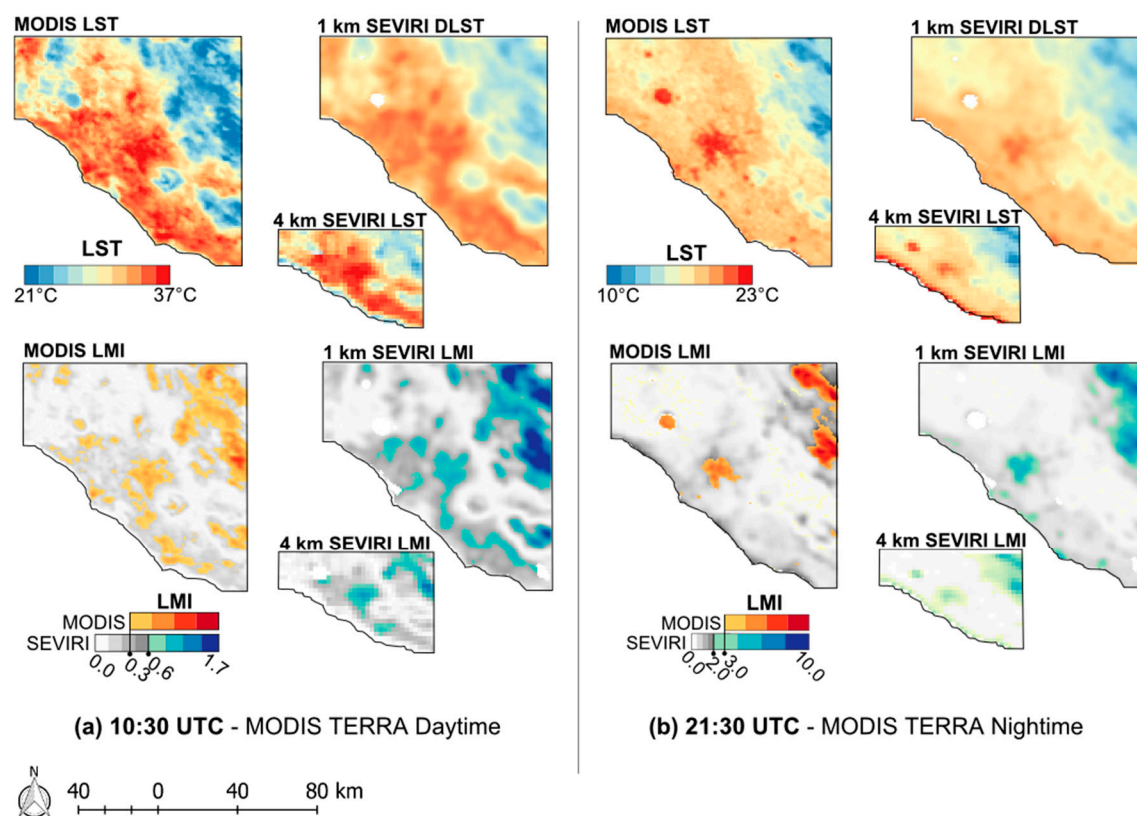
Figure 8. The three-month mean MODIS LST and MSG3-SEVIRI LST and DLST images for (**a**) 10:30 UTC and (**b**) 21:30 UTC. The corresponding LMI images are also presented, and the prevalent thermal clusters are highlighted (tones of blue for MSG3-SEVIRI and tones of red for MODIS).

4.3. Assessment of the DLST Spatiotemporal Features

4.3.1. Assessment of the DLST Spatial Pattern Diurnal Evolution

In Figure 9, the diurnal evolution of the 4-km LST-derived LMI and the corresponding 1-km DLST-derived LMI is presented. According to the 4-km LMI data, the study area's diurnal cycle can be perceived as a five-phase cycle. During the first phase, the Apennine Mountains and Rome's SUHI effect are the prevalent LST spatial features (the former remains strong throughout Phase 1 and also the entire day, while the latter weakens with the passage of time). In Phase 2, the rural region becomes a prevalent thermal cluster that is warmer than the city of Rome, and thus, an urban sink phenomenon occurs [48]. In Phase 3, the most complex LST patterns occur: at 10:30 UTC, the eastern part of Rome forms a well-defined cluster that is warmer than the western part and stands out from the surrounding rural area, while at 13:30 UTC, the east and west parts of Rome have similar LST values and form a unified cluster centered over Rome. During Phase 4, the LST values start to drop, and the rural thermal pattern weakens until it disappears. The cluster corresponding to Rome shrinks, but remains prevalent. In the last phase, the predominant spatial patterns are those induced by the mountainous region and Rome's SUHI, similar to Phase 1 (Figure 9, 19:30 and 22:30 UTC). The success of the downscaling process depends on how well the DLST time series can emulate the characteristics of the aforementioned diurnal cycle.
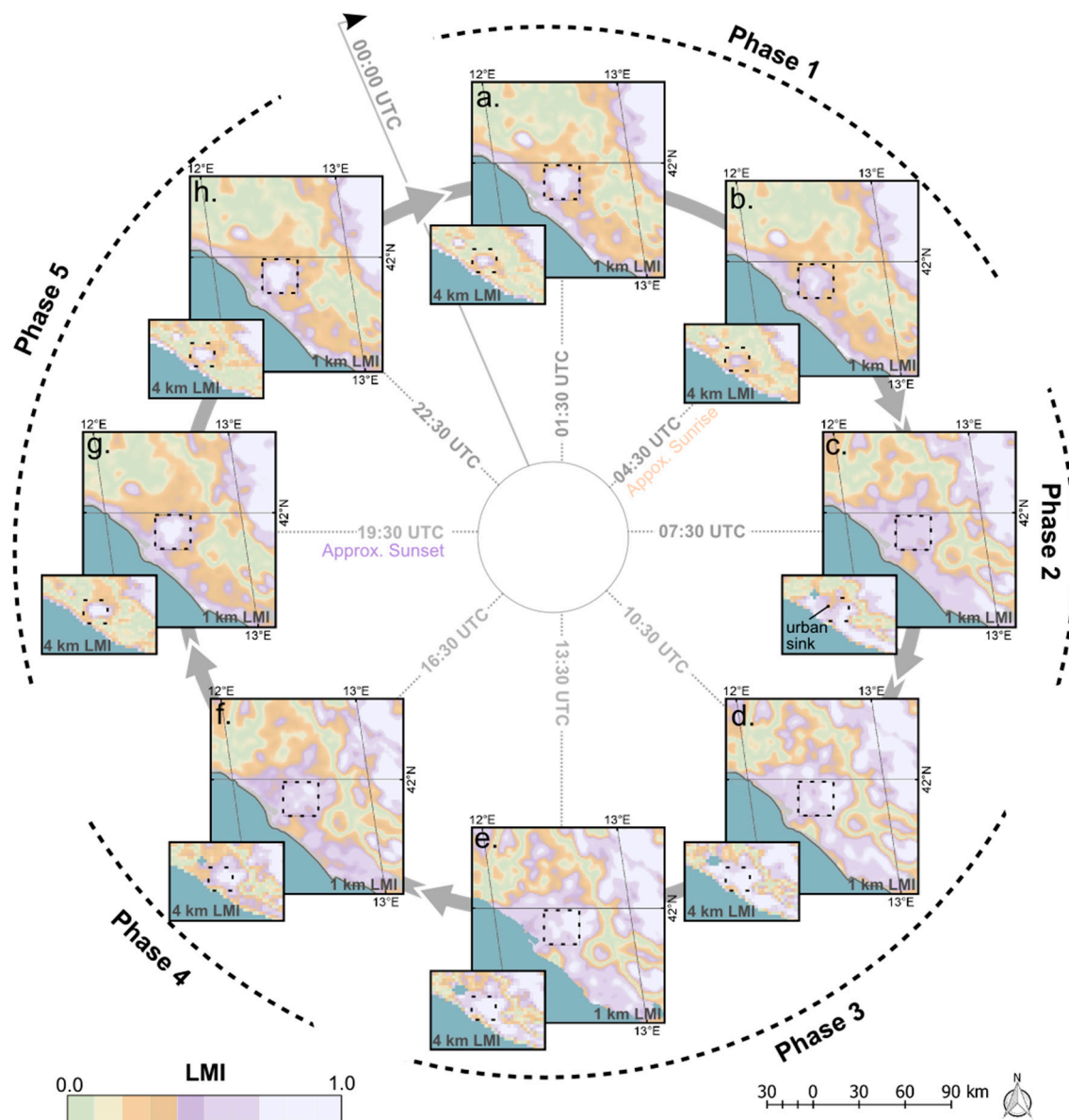
Figure 9. The diurnal evolution of the 4-km and 1-km MSG3-SEVIRI LMI (the LMI were min-max normalized separately). The black squares correspond to the city of Rome, Italy.

In general, the diurnal evolution of the DLST spatial patterns follows the five-phase cycle discussed above. However, the DLST scheme did not reproduce the urban sink phenomenon observed for the 4-km 07:30 UTC LMI image (Figure 9c). This is an important issue, because it can adversely impact the analysis of the SUHI diurnal evolution. Another issue observed is that the strength of the diurnal spatial changes is weaker in the generated DLST data than in the original MSG3-SEVIRI LST data, as Figure 7d,e reveals. Specifically, the Phase 2, 3 and 4 Rho values corresponding to the DLST data are considerably higher than the reference data (yellow curves, Figure 7). This finding suggests that the increased similarity of the DLST data made the diurnal cycle changes less pronounced and, thus, the generated daytime and nighttime DLST data more similar. Finally, Figure 7f,g shows that the diurnal evolution of the DLST data is smooth as Rho is equal to ~1 for every case. In that figure, at the time spots where the ACPs change takes place, a minor drop of 0.02 (Rho ≈ 0.98) is observable that is deemed not important. Hence, it can be suggested that the use of a large number of LST predictors with an SVM was able to compensate the sudden change of LST predictors.

4.3.2. Assessment of the DLST Potential to Emulate LST Temporal Features

The last stage of the evaluation process is the assessment of the DLST time series' potential to emulate the temporal features of the original 4-km LST time series. In Figure 10, the mean, minimum and maximum LST and DLST values for each image of the original MSG3-SEVIRI 4-km and the generated 1-km datasets are presented for the period under study (Summer 2014). The retrieved 4-km LST and 1-km DLST values are very similar and form a sine-wave pattern. These two characteristics suggest that the DLST data adequately preserved the radiometry of the original data and, thus, were capable of retaining the smooth increases and decreases of the measured 4-km LST values.
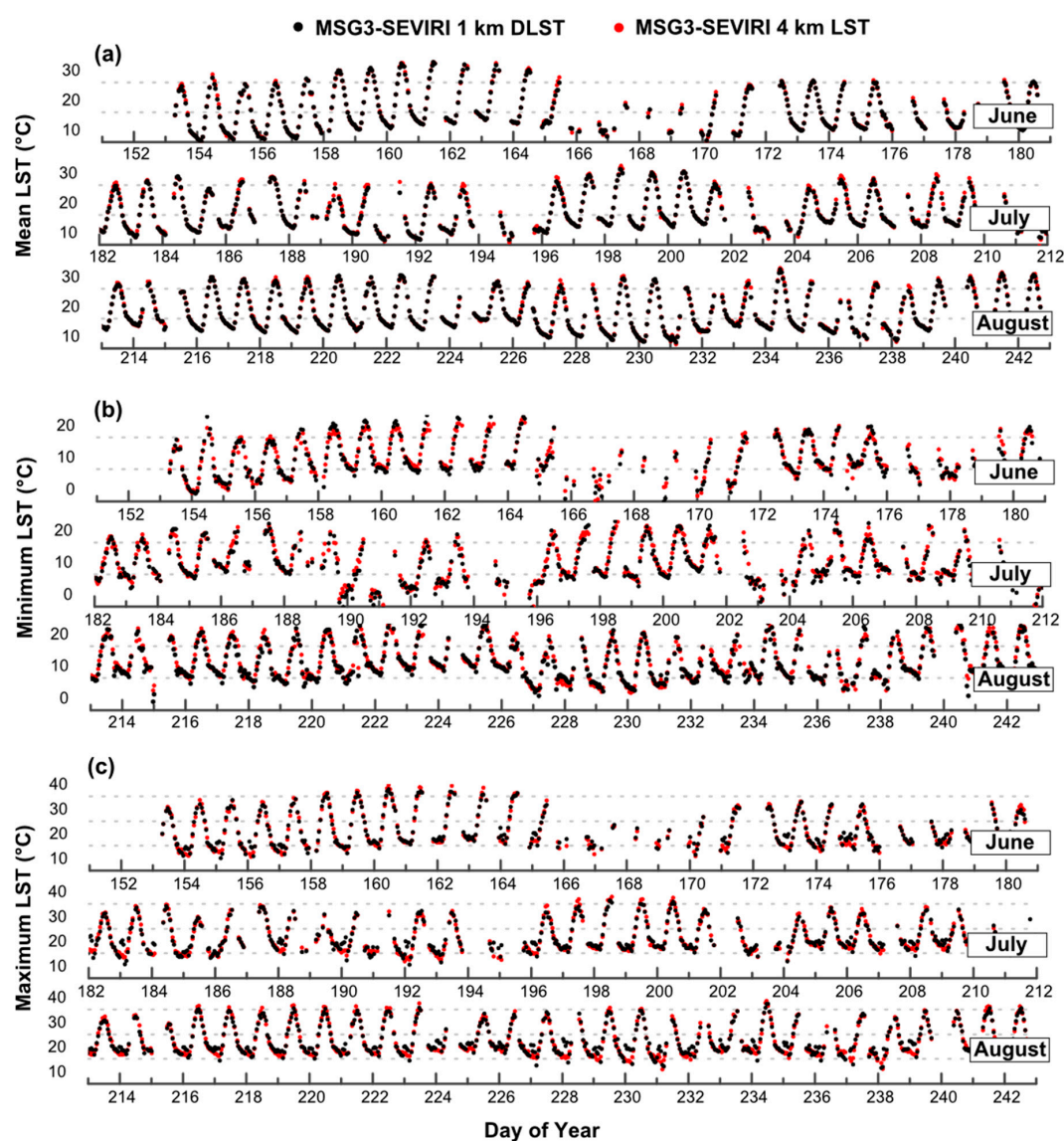

Figure 10. Juxtaposition of the (**a**) mean; (**b**) minimum and (**c**) maximum MSG3-SEVIRI LST and DLST values of the original 4-km and the generated 1-km datasets for summer 2014.

The long-term seasonal effects on the DLST spatial patterns are studied in Figure 11 by estimating the Rho between the first image of each employed dataset (*i.e.*, the MODIS LST and MSG3-SEVIRI DLST time series) and the rest (as discussed in Section 3.2.3 and presented in Figure 3a). Specifically, the expected declining Rho trend due to the seasonal effects is observable only for the daytime data, but very weakly (Figure 11b,c). For the nighttime data, the linear fits (Figure 11a–d) are almost horizontal

(the slight increasing MODIS trend in Figure 11d is an artifact caused by the availability of more image data after DOY 190). This is mostly due to the fact that the utilized data correspond to the same season of the year. The most interesting observation though concerns the magnitude of the Rho values obtained. Specifically, the MODIS Rho values are lower (by 0.1–0.2) than the ones derived from the MSG3-SEVIRI DLST dataset. This observation hints that the generated DLST spatial patterns are more similar than the measured LST data (a similar issue was noticed when the daytime and nighttime DLST spatial patterns were compared in Section 4.3.1) and that the downscaling process could not represent the spatial thermal changes as pronouncedly as the measured data could.
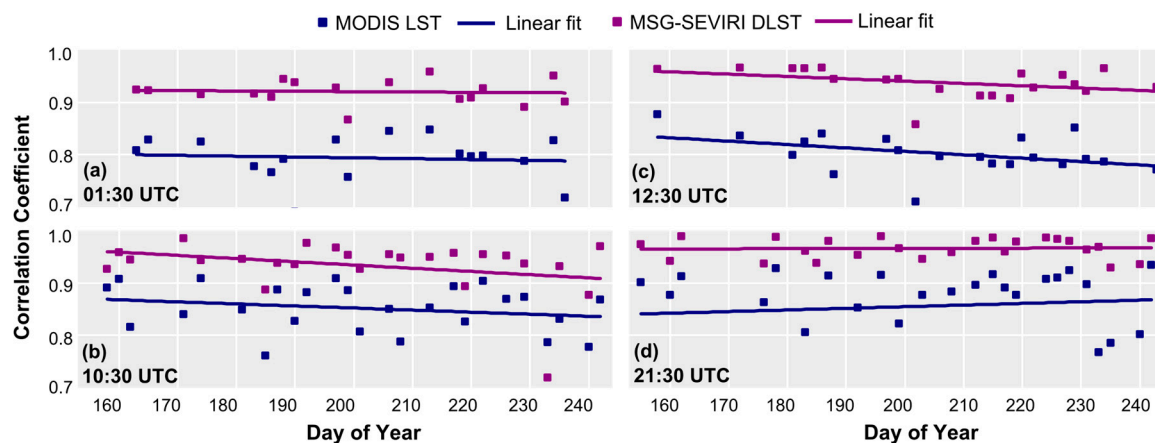

Figure 11. The (**a**) 01:30 UTC; (**b**) 10:30 UTC; (**c**) 12:30 UTC, and 21:30 UTC Rho between the first LST/DLST image of each dataset and the rest.

5. Conclusions

The downscaling of frequently-acquired geostationary LST has the potential to compensate the lack of high spatiotemporal LST time series for urban climate studies. To deem the downscaling of geostationary LST time series successful and capable of capturing the spatial and temporal variations of SUHIs, the generated high spatiotemporal DLST time series must reproduce the spatiotemporal features of the coarse-scale LST time series with greater spatial detail. This is one of the first studies that discusses this issue and assesses if the generated DLST data can indeed be exploited in urban thermal applications. To address this question, this work studied the accuracy, the correct pattern formation and the temporal changes of a downscaled three month-long MSG3-SEVIRI LST time series depicting the city of Rome, Italy.

The results suggest that the downscaling process operated in a consistent manner, preserved the radiometry of the original MSG3-SEVIRI data and generated noon, afternoon and nighttime spatial thermal patterns that were similar to those present in the evaluation data. However, the evaluation revealed that the generated DLST data could not emulate the morning urban sink of Rome, which is an important issue for SUHI studies. Moreover, the results also suggest that the downscaling of urban pixels is more challenging than for rural pixels, both for daytime and nighttime images. In particular, the evaluation process showed that the diurnal evolution of the generated data was smooth, but the autocorrelation of the 1-km DLST data was higher than of the original 4-km LST data. This suggests that the DLST data could not present subtle spatial thermal changes during the course of a day as pronouncedly as the measured data could. These findings (even though confined to this study) reveal a series of issues that are important to urban thermal studies that using only conventional DLST evaluating schemes (*i.e.*, comparisons with independent LST data confined to certain time spots) would remain unrevealed.

Generalizing the aforementioned observations, the assessment of high spatiotemporal DLST data for urban thermal applications should consider also the following issues:

- The capability of the DLST data to accurately emulate the SUHI diurnal pattern cycle.
- The capability to detect subtle spatial thermal changes during the course of a day.
- The smoothness of the diurnal evolution of the DLST data.
- The consistent performance of the employed downscaling method.

The exploitation of the DLST data spatiotemporal inter-relationship for evaluation purposes can overcome some of the limitations posed by the lack of ground truth data and facilitate the assessment of the issues listed above. Presently, this matter is overlooked. However, the capability of the downscaling process to accurately emulate the DLST diurnal cycle values and patterns and the time series' temporal characteristics is crucial. This is because these two features ultimately determine the exploitability of the DLST time series for generating added value products and services for the study of the urban thermal environment, such as the estimation of air temperature, the SUHI analysis and the heat wave hazard assessment.

Besides the difficulties and the limitations currently faced, the generation of geostationary DLST time series is an important advancement of TIR remote sensing that can facilitate the study of the urban climate. Future research should focus more on the assessment of the spatiotemporal characteristics of DLST time series.

Author Contributions: P.S. conceived of, designed and performed the experiments and wrote the paper. I.K. and C.T.K. developed the IAASARS/NOA system that produces the DLST data and reviewed the paper. B.B. produced the ACPs and reviewed the paper.

Conflicts of Interest: The authors declare no conflict of interest.

Abbreviations

The following abbreviations are used in this manuscript:

ACPs	Annual Cycle Parameters
DLST	Downscaled Land Surface Temperature
DOY	Day of Year
EVI	Enhanced Vegetation Index
IAASARS/NOA	Institute for Astronomy, Astrophysics, Space Applications and Remote Sensing, National Observatory of Athens
LMI	Local Moran Index
LST	Land Surface Temperature
MAST	Mean Annual Surface Temperature
MODIS	Moderate Resolution Imaging Spectroradiometer
MSG3-SEVIRI	Meteosat Second Generation 3–Spinning Enhanced Visible and Infrared Imager
NDVI	Normalized Difference Vegetation Index
NNs	Neural Networks
Rho	Pearson's correlation coefficient
RMSE	Root-Mean-Square-Error
SD	Standard Deviation
SRTM	Shuttle Radar Topography Mission
SVM	Support Vector Regression Machine
SUHI	Surface Urban Heat Island

TA	Air Temperature
TIR	Thermal Infrared
UHI	Urban Heat Island
UTC	Coordinated Universal Time
VIs	Vegetation Indices
VZA	View Zenith Angle
YAST	Yearly Amplitude of Surface Temperature
ε	Spectral emissivity
θ	Phase shift

References

1. Oke, T. The Energetic Basis of the Urban Heat Island. *Q. J. R. Meteorol. Soc.* **1982**, *108*, 1–24. [CrossRef]
2. Mihalakakou, G.; Santamouris, M.; Papanikolaou, N.; Cartalis, C.; Tsangrassoulis, A. Simulation of the Urban Heat Island Phenomenon in Mediterranean Climates. *Pure Appl. Geophys.* **2004**, *161*, 429–451. [CrossRef]
3. Deng, C.; Wu, C. Examining the Impacts of Urban Biophysical Compositions on Surface Urban Heat Island: A Spectral Unmixing and Thermal Mixing Approach. *Remote Sens. Environ.* **2013**, *131*, 262–274. [CrossRef]
4. Taylor, J.; Wilkinson, P.; Davies, M.; Armstrong, B.; Chalabi, Z.; Mavrogianni, A.; Symonds, P.; Oikonomou, E.; Bohnenstengel, S.I. Mapping the Effects of Urban Heat Island, Housing, and Age on Excess Heat-Related Mortality in London. *Urban Clim.* **2015**, *14*, 1–12. [CrossRef]
5. Clinton, N.; Gong, P. MODIS Detected Surface Urban Heat Islands and Sinks: Global Locations and Controls. *Remote Sens. Environ.* **2013**, *134*, 294–304. [CrossRef]
6. Akbari, H.; Davis, S.; Dorsano, S.; Huang, J.; Winnett, S. *Cooling Our Communities a Guidebook on Tree Planting and Light-Colored Surfacing*; Environmental Protection Agency: Washington, DC, USA, 1992.
7. Kim, Y.-H.; Baik, J.-J. Spatial and Temporal Structure of the Urban Heat Island in Seoul. *J. Appl. Meteorol.* **2005**, *44*, 591–605. [CrossRef]
8. Bornstein, R. Observations of the Urban Heat Island Effect in New York City. *J. Appl. Meteorol.* **1968**, *7*, 575–582. [CrossRef]
9. Jones, P.D.; Lister, D.H. The Urban Heat Island in Central London and Urban-Related Warming Trends in Central London since 1900. *Weather* **2009**, *64*, 323–327. [CrossRef]
10. Stathopoulou, M.; Cartalis, C. Daytime Urban Heat Islands from Landsat ETM+ and Corine Land Cover Data: An Application to Major Cities in Greece. *Sol. Energy* **2007**, *81*, 358–368. [CrossRef]
11. Liu, L.; Zhang, Y. Urban Heat Island Analysis Using the Landsat TM Data and ASTER Data: A Case Study in Hong Kong. *Remote Sens.* **2011**, *3*, 1535–1552. [CrossRef]
12. Kato, S.; Yamaguchi, Y. Analysis of Urban Heat-Island Effect Using ASTER and ETM+ Data: Separation of Anthropogenic Heat Discharge and Natural Heat Radiation from Sensible Heat Flux. *Remote Sens. Environ.* **2005**, *99*, 44–54. [CrossRef]
13. Rao, M.K. Remote Sensing of Urban "Heat Islands" from an Environmental Satellite. *Bull. Am. Meteorol. Soc.* **1972**, *53*, 647–648.
14. Price, J. Assessment of the Urban Heat Island Effect through the Use of Satellite Data. *Mon. Weather Rev.* **1979**, *107*, 1554–1557. [CrossRef]
15. Roth, M.; Oke, T.R.; Emery, W.J. Satellite-Derived Urban Heat Islands from Three Coastal Cities and the Utilization of Such Data in Urban Climatology. *Int. J. Remote Sens.* **1989**, *10*, 1699–1720. [CrossRef]
16. Voogt, J.A.; Oke, T. Thermal Remote Sensing of Urban Climates. *Remote Sens. Environ.* **2003**, *86*, 370–384. [CrossRef]
17. Sismanidis, P.; Keramitsoglou, I.; Kiranoudis, C.T. Evaluating the Operational Retrieval and Downscaling of Urban Land Surface Temperatures. *IEEE Geosci. Remote Sens. Lett.* **2015**, *12*, 1312–1316. [CrossRef]
18. Weng, Q. Thermal Infrared Remote Sensing for Urban Climate and Environmental Studies: Methods, Applications, and Trends. *ISPRS J. Photogramm. Remote Sens.* **2009**, *64*, 335–344. [CrossRef]
19. Imhoff, M.L.; Zhang, P.; Wolfe, R.E.; Bounoua, L. Remote Sensing of the Urban Heat Island Effect across Biomes in the Continental USA. *Remote Sens. Environ.* **2010**, *114*, 504–513. [CrossRef]
20. Keramitsoglou, I.; Kiranoudis, C.T.; Ceriola, G.; Weng, Q.; Rajasekar, U. Identification and Analysis of Urban Surface Temperature Patterns in Greater Athens, Greece, Using MODIS Imagery. *Remote Sens. Environ.* **2011**, *115*, 3080–3090. [CrossRef]

21. Li, Z.-L.; Tang, B.-H.; Wu, H.; Ren, H.; Yan, G.; Wan, Z.; Trigo, I.F.; Sobrino, J.A. Satellite-Derived Land Surface Temperature: Current Status and Perspectives. *Remote Sens. Environ.* **2013**, *131*, 14–37. [CrossRef]

22. Zakšek, K.; Oštir, K. Downscaling Land Surface Temperature for Urban Heat Island Diurnal Cycle Analysis. *Remote Sens. Environ.* **2012**, *117*, 114–124. [CrossRef]

23. Keramitsoglou, I.; Kiranoudis, C.T.; Weng, Q. Downscaling Geostationary Land Surface Temperature Imagery for Urban Analysis. *IEEE Geosci. Remote Sens. Lett.* **2013**, *10*, 1253–1257. [CrossRef]

24. Bechtel, B.; Zakšek, K.; Hoshyaripour, G. Downscaling Land Surface Temperature in an Urban Area: A Case Study for Hamburg, Germany. *Remote Sens.* **2012**, *4*, 3184–3200. [CrossRef]

25. Weng, Q.; Fu, P. Modeling Diurnal Land Temperature Cycles over Los Angeles Using Downscaled GOES Imagery. *ISPRS J. Photogramm. Remote Sens.* **2014**, *97*, 78–88. [CrossRef]

26. Zhan, W.; Chen, Y.; Zhou, J.; Wang, J.; Liu, W.; Voogt, J.; Zhu, X.; Quan, J.; Li, J. Disaggregation of Remotely Sensed Land Surface Temperature: Literature Survey, Taxonomy, Issues, and Caveats. *Remote Sens. Environ.* **2013**, *131*, 119–139. [CrossRef]

27. Agam, N.; Kustas, W.P.; Anderson, M.C.; Li, F.; Neale, C.M.U. A Vegetation Index Based Technique for Spatial Sharpening of Thermal Imagery. *Remote Sens. Environ.* **2007**, *107*, 545–558. [CrossRef]

28. Kustas, W.P.; Norman, J.M.; Anderson, M.C.; French, A.N. Estimating Subpixel Surface Temperatures and Energy Fluxes from the Vegetation Index–radiometric Temperature Relationship. *Remote Sens. Environ.* **2003**, *85*, 429–440. [CrossRef]

29. Inamdar, A.K.; French, A.; Hook, S.; Vaughan, G.; Luckett, W. Land Surface Temperature Retrieval at High Spatial and Temporal Resolutions over the Southwestern United States. *J. Geophys. Res.* **2008**, *113*, 1–18. [CrossRef]

30. Sun, D.; Kafatos, M. Note on the NDVI-LST Relationship and the Use of Temperature-Related Drought Indices over North America. *Geophys. Res. Lett.* **2007**, *34*, 1–4. [CrossRef]

31. Jeganathan, C.; Hamm, N.A.S.; Mukherjee, S.; Atkinson, P.M.; Raju, P.L.N.; Dadhwal, V.K. Evaluating a Thermal Image Sharpening Model over a Mixed Agricultural Landscape in India. *Int. J. Appl. Earth Obs. Geoinf.* **2011**, *13*, 178–191. [CrossRef]

32. Wu, P.; Shen, H.; Zhang, L.; Göttsche, F.-M. Integrated Fusion of Multi-Scale Polar-Orbiting and Geostationary Satellite Observations for the Mapping of High Spatial and Temporal Resolution Land Surface Temperature. *Remote Sens. Environ.* **2015**, *156*, 169–181. [CrossRef]

33. Weng, Q.; Fu, P.; Gao, F. Generating Daily Land Surface Temperature at Landsat Resolution by Fusing Landsat and MODIS Data. *Remote Sens. Environ.* **2014**, *145*, 55–67. [CrossRef]

34. Bechtel, B. Robustness of Annual Cycle Parameters to Characterize the Urban Thermal Landscapes. *IEEE Geosci. Remote Sens. Lett.* **2012**, *9*, 876–880. [CrossRef]

35. Bechtel, B. A New Global Climatology of Annual Land Surface Temperature. *Remote Sens.* **2015**, *7*, 2850–2870. [CrossRef]

36. Bechtel, B.; Böhner, J.; Zakšek, K.; Wiesner, S. Downscaling of Diurnal Land Surface Temperature Cycles for Urban Heat Island Monitoring. In Proceedings of the Joint Urban Remote Sensing Event, Sao Paolo, Brazil, 21–23 April 2013.

37. Verbesselt, J.; Zeileis, A.; Herold, M. Near Real-Time Disturbance Detection Using Satellite Image Time Series. *Remote Sens. Environ.* **2012**, *123*, 98–108. [CrossRef]

38. Tan, J.; Zheng, Y.; Tang, X.; Guo, C.; Li, L.; Song, G.; Zhen, X.; Yuan, D.; Kalkstein, A.J.; Li, F. The Urban Heat Island and Its Impact on Heat Waves and Human Health in Shanghai. *Int. J. Biometeorol.* **2010**, *54*, 75–84. [CrossRef] [PubMed]

39. Lo, C.P.; Quattrochi, D.A.; Luvall, J.C. Application of High-Resolution Thermal Infrared Remote Sensing and GIS to Assess the Urban Heat Island Effect. *Int. J. Remote Sens.* **2010**, *18*, 287–304. [CrossRef]

40. Julien, Y.; Sobrino, J.A. The Yearly Land Cover Dynamics (YLCD) Method: An Analysis of Global Vegetation from NDVI and LST Parameters. *Remote Sens. Environ.* **2009**, *113*, 329–334. [CrossRef]

41. Sismanidis, P.; Keramitsoglou, I.; Kiranoudis, C.T. A Satellite-Based System for Continuous Monitoring of Surface Urban Heat Islands. *Urban Clim.* **2015**, *14*, 141–153. [CrossRef]

42. Trigo, I.F.; Monteiro, I.T.; Olesen, F.; Kabsch, E. An Assessment of Remotely Sensed Land Surface Temperature. *J. Geophys. Res.* **2008**, *113*, D17108. [CrossRef]

43. Rabus, B.; Eineder, M.; Roth, A.; Bamler, R. The Shuttle Radar Topography Mission-A New Class of Digital Elevation Models Acquired by Spaceborne Radar. *ISPRS J. Photogramm. Remote Sens.* **2003**, *57*, 241–262. [CrossRef]

44. Arino, O.; Gross, D.; Ranera, F.; Bourg, L.; Leroy, M.; Bicheron, P.; Latham, J.; Di Gregorio, A.; Brockman, C.; Witt, R.; *et al*. GlobCover: ESA Service for Global Land Cover from MERIS. In *Geoscience and Remote Sensing Symposium*; IEEE: Barcelona, Spain, 2007; pp. 2412–2415. [CrossRef]

45. Mountrakis, G.; Im, J.; Ogole, C. Support Vector Machines in Remote Sensing: A Review. *ISPRS J. Photogramm. Remote Sens.* **2010**, *66*, 259–247. [CrossRef]

46. Anselin, L. Local Indicators of Spatial Association—LISA. *Geogr. Anal.* **1995**, *27*, 93–115. [CrossRef]

47. Voogt, J.; Oke, T. Complete Urban Surface Temperatures. *J. Appl. Meteorol.* **1997**, *36*, 1117–1132. [CrossRef]

48. Fabrizi, R.; Bonafoni, S.; Biondi, R. Satellite and Ground-Based Sensors for the Urban Heat Island Analysis in the City of Rome. *Remote Sens.* **2010**, *2*, 1400–1415. [CrossRef]